

RESEARCH ARTICLE

10.1002/2016JA022706

Compressional ULF wave modulation of energetic particles in the inner magnetosphere

H. Liu¹, Q.-G. Zong¹, X.-Z. Zhou¹, S. Y. Fu¹, R. Rankin², L.-H. Wang¹, C. J. Yuan¹, Y. F. Wang¹, D. N. Baker³, J. B. Blake⁴, and C. A. Kletzing⁵¹Institute of Space Physics and Applied Technology, Peking University, Beijing, China, ²Department of Physics, University of Alberta, Edmonton, Alberta, Canada, ³Laboratory for Atmospheric and Space Physics, University of Colorado Boulder, Boulder, Colorado, USA, ⁴The Aerospace Corporation, Los Angeles, California, USA, ⁵Department of Physics and Astronomy, University of Iowa, Iowa City, Iowa, USA

Key Points:

- We present an event about compressional ULF wave modulation of energetic particles observed by Van Allen Probes on 19 February 2014
- The modulation extends across a wide range of energies, from 79.80 to 2850 keV for electrons and from 82.85 to 636.18 keV for protons
- The modulation is ascribed to mirror effect, and the peak-to-valley ratios of fluxes are determined by shapes of pitch angle distributions

Correspondence to:

Q.-G. Zong,
qgzong@pku.edu.cn

Citation:

Liu, H., et al. (2016), Compressional ULF wave modulation of energetic particles in the inner magnetosphere, *J. Geophys. Res. Space Physics*, 121, 6262–6276, doi:10.1002/2016JA022706.

Received 16 MAR 2016

Accepted 25 MAY 2016

Accepted article online 30 MAY 2016

Published online 9 JUL 2016

Abstract We present Van Allen Probes observations of modulations in the flux of very energetic electrons up to a few MeV and protons between 1200 and 1400 UT on 19 February 2014. During this event the spacecraft were in the dayside magnetosphere at $L^* \approx 5.5$. The modulations extended across a wide range of particle energies, from 79.80 keV to 2.85 MeV for electrons and from 82.85 keV to 636.18 keV for protons. The fluxes of $\pi/2$ pitch angle particles were observed to attain maximum values simultaneously with the ULF compressional magnetic field component reaching a minimum. We use peak-to-valley ratios to quantify the strength of the modulation effect, finding that the modulation is larger at higher energies than at lower energies. It is shown that the compressional wave modulation of the particle distribution is due to the mirror effect, which can trap relativistic electrons efficiently for energies up to 2.85 MeV and trap protons up to ≈ 600 keV. Larger peak-to-valley ratios at higher energies also attributed to the mirror effect. Finally, we suggest that protons with energies higher than 636.18 keV cannot be trapped by the compressional ULF wave efficiently due to the finite Larmor radius effect.

1. Introduction

Ultralow frequency (ULF) magnetic pulsations were first recorded at geomagnetic stations in the middle nineteenth century [Stewart, 1861]. Since then numerous observations have been reported based on both ground and space measurements, divided into subgroups by frequency [Jacobs *et al.*, 1964]. A variety of mechanisms have been developed to explain the different frequency, polarization, and propagation characteristics of these waves [e.g., Lee and Lysak, 1989].

Magnetic pulsations can be decomposed into compressional and transverse parts. Spacecraft in situ measurements on both waves and energetic particles provide a possibility to analyze the compressional wave modulation of particles. Storm time compressional ULF waves have been reported with correlative particle motions during the main phase of a geomagnetic storm [Brown *et al.*, 1968; Sonnerup *et al.*, 1969; Lanzerotti *et al.*, 1969; Walker *et al.*, 1982]. A compressional ULF wave event under a moderate solar wind condition has also been reported [Higbie *et al.*, 1982; Nagano and Araki, 1983]. Kremser *et al.* [1981] found 54 compressional wave modulation events of two main types between August 1978 and July 1979. They found that ion and electron fluxes oscillate in phase in one type and out of phase in the other type. The in-phase events occurred preferentially around noon with pitch angle distributions peaking at $\pi/2$; the out-of-phase events usually correspond to “butterfly” electron distributions.

Compressional ULF waves have been observed to propagate westward [Takahashi *et al.*, 1985] or eastward [Takahashi *et al.*, 1987] at several km/s. However, the nature of their excitation remains unsolved. Kremser *et al.* [1981] pointed out that the drift mirror instability offers a potential explanation of the in-phase and out-of-phase events though the instability criteria are not examined. Higbie *et al.* [1982] listed several potential mechanisms to produce these oscillations, such as solar wind-driven magnetospheric fluctuating waves, drift mode instability in high- β plasma, and coupling between the magnetosphere and ionosphere. Takahashi *et al.* [1985] excluded the possibility of external source mechanisms and suggested that plasma pressure anisotropy, revealed by particle pitch angle distributions, is large enough to trigger the drift mirror wave. This mechanism was first suggested by Hasegawa [1969] and is supported by theory [e.g., Walker *et al.*, 1982;

Southwood and Kivelson, 1993; Kivelson and Southwood, 1996] and observations [Rae et al., 2007; Sibeck et al., 2012] in the context of the magnetosphere.

Lin et al. [1976] developed a model to analyze particle flux responses to compressional ULF waves. Under the assumption that the first, second, and third adiabatic invariants are conserved, they found that Betatron and Fermi acceleration processes can lead to an increase in the $\pi/2$ pitch angle flux when the local magnetic field is enhanced. Kivelson and Southwood [1985] discussed charged particle behavior in compressional ULF waves with the form $b_{\parallel} \exp(im\phi - i\omega t)$ and showed that modulations in particle flux can be dominated by the “mirror effect.” Zhu and Kivelson [1994] examined an event observed by the ISEE spacecraft in duskside magnetosphere and also regarded the mirror effect as a probable mechanism. However, relativistic electron responses to compressional ULF waves in the inner magnetosphere are not addressed yet due to lack of observations. This paper represents such an observation and provides a new sight on interaction between compressional waves and relativistic electrons. In section 4, we give quantitative descriptions of mirror effect for different pitch angle distributions and give an explicit explanation of in-phase and out-of-phase events refer to Kremser et al. [1981].

2. Instrumentation

The twin Van Allen Probes spacecraft were launched into nearly identical orbits on August 2012 with a perigee of $\approx 1.1 R_E$, an apogee of $\approx 5.8 R_E$, and an inclination of $\approx 10^\circ$. In the observations reported here, i.e., 1200–1400 UT on 19 February 2014, combined instruments are used to analyze the magnetic field modulation of energetic particles, including Electric and Magnetic Field Instrument Suite and Integrated Science (EMFISIS) [Kletzing et al., 2013], Relativistic Electron-Proton Telescope (REPT) investigation [Baker et al., 2012], and Magnetic Electron Ion Spectrometer (MagEIS) [Blake et al., 2013]. Solar wind parameters are obtained from the Magnetic Field Investigation (MFI) [Lepping et al., 1995] and Solar Wind Experiment (SWE) [Ogilvie et al., 1995] instruments onboard the Wind satellite, which was launched on 1 November 1994 and placed in a halo orbit near the solar terrestrial space Lagrange 1 point, more than $200 R_E$ from the Earth. The *Dst* index is taken from World Data Center for Geomagnetism, Kyoto (<http://wdc.kugi.kyoto-u.ac.jp/index.html>).

3. Observations

3.1. Solar Wind Conditions

Figure 1 shows the solar wind conditions from 0000 to 2400 UT on 19 February 2014. The Wind satellite was situated at around $(210.5 R_E, 95.5 R_E, \text{ and } -5.8 R_E)$ in the GSM coordinate system near the Lagrange 1 point, about $231.2 R_E$ away from the geocenter. Figures 1a–1c show B_x , B_z components, and total intensity B_t of the interplanetary magnetic field (IMF); Figures 1d and 1e show the solar wind velocity V_s and ion dynamic pressure P_i , respectively. The solar wind conditions changed dramatically at ≈ 0300 UT, with sudden enhancements of southward B_z , magnitude B_t , and V_s . Since the IMF was strongly southward before ≈ 0300 UT and a weak storm was already underway, these changes of IMF conditions at ≈ 0300 UT initiated a second dip in the *Dst* index formed a double dip storm, as presented in Figure 2. After reaching a minimum, the *Dst* index began to increase at about 0900 UT. The time interval of interest, 1200–1400 UT, was in the recovery phase of the storm, during which the IMF B_z gradually increased to ≈ 10 nT, the solar wind velocity increased from 450 km/s at 1000 UT to 500 km/s at about 1230 UT, and the ion dynamic pressure at ≈ 1200 UT showed an enhancement, cf. Figure 1.

3.2. Van Allen Probes Magnetic Field and Particle Flux

The orbit trajectories of Van Allen Probes A and B between 0800 and 1600 UT on 19 February 2014 are shown in Figure 3, where the red line represents Van Allen Probe A and the blue line represents Van Allen Probe B. The red solid dot marked “12” represents the location of Van Allen Probe A at 1200 UT in the XY plane of the Solar Magnetic (SM) coordinates. It is shown that Van Allen Probe A passes apogee at around 1240 UT, and Van Allen Probe B passes apogee at around 1110 UT. Note that the inclination for the two spacecrafts are only $\approx 10^\circ$, and so the magnetic field in this region is expected to be dipolar.

We focus first on Van Allen Probe A observations of magnetic field and particle fluxes. Figure 4 (left column) shows the magnetic field in GSM coordinates between 1200 and 1400 UT. Figure 4g (left column) shows the magnetic position of the spacecraft between $L^* \approx 5.1 - 5.4$, magnetic local time $\approx 11 - 13$, and MLAT (magnetic latitude) $\approx -6^\circ - -2^\circ$. Figures 4a–4c (left column) show the three components of the magnetic field in GSM, where B_x and B_y are close to zero as the spacecraft is near the magnetic equator, but B_z remains

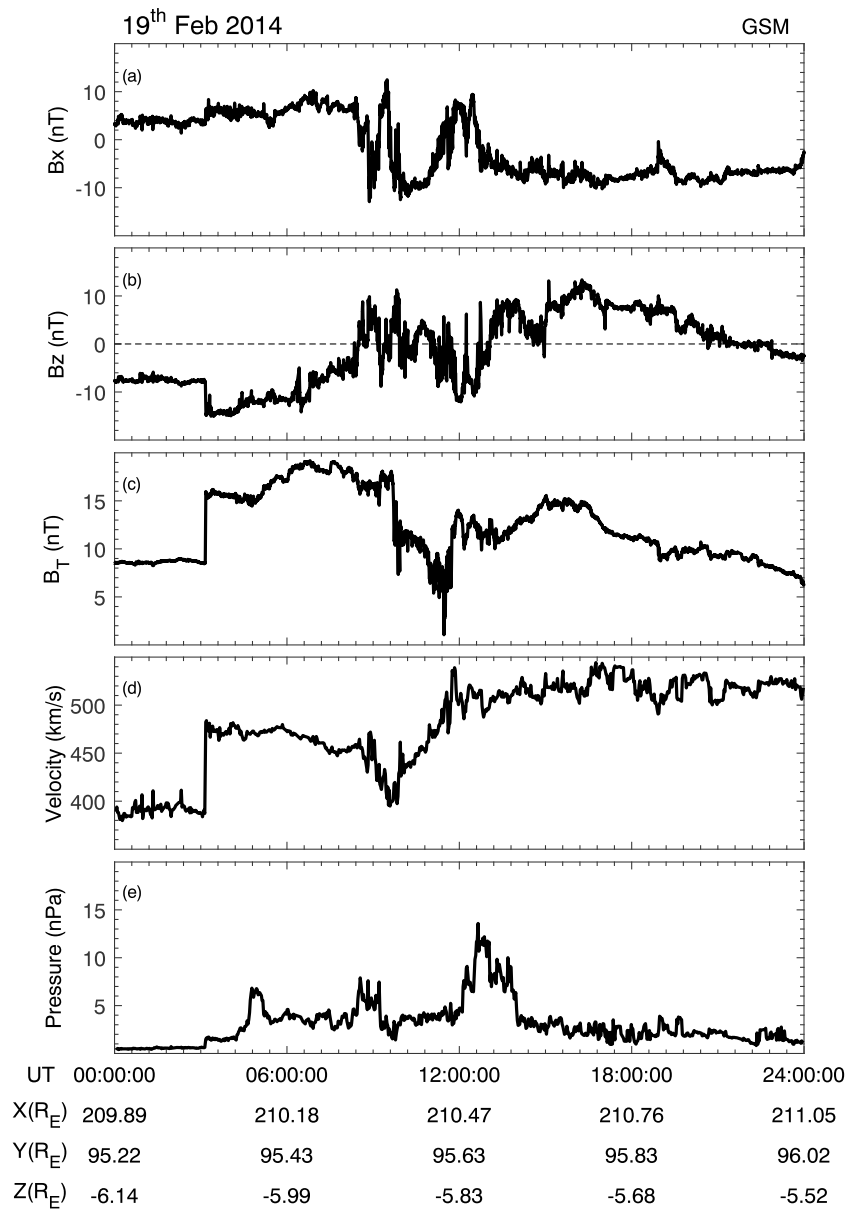


Figure 1. Solar wind parameters observed by Wind satellite on 19 February 2014, 0000–2400 UT in GSM coordinates. (a–e) Interplanetary magnetic field including B_x , B_z , B_T , solar wind velocity, and ion dynamic pressure are plotted, when the Wind satellite was situated at $(210.5R_E, 95.5R_E, \text{ and } -5.8R_E)$ near the Lagrange 1 point.

≈ 180 nT. Figures 4d–4f (left column) show the detrended components of the magnetic field corresponding to Figures 4a–4c (left column), respectively; they are obtained by subtracting 20 min smooth averages.

Although the magnetic field is dipole-like between 1200 and 1400 UT, there are clear perturbations superposed on the background trend. The magnetic field is projected onto a mean field-aligned (MFA) coordinate system [Zong *et al.*, 2009] to distinguish different wave modes. In the MFA system the coordinate axes point in the radial (outward), azimuthal (eastward), and parallel direction, respectively. The parallel direction is determined by 20 min sliding averaged magnetic field. The radial direction lies in the plane containing the field-aligned and geocentric radius vectors and points away from the Earth. The azimuthal direction completes the right-handed orthogonal set. Oscillations in the three directions can be divided into toroidal, poloidal, and compressional modes, and the compressional mode will contain a diagnostic parallel component as well as a radial component.

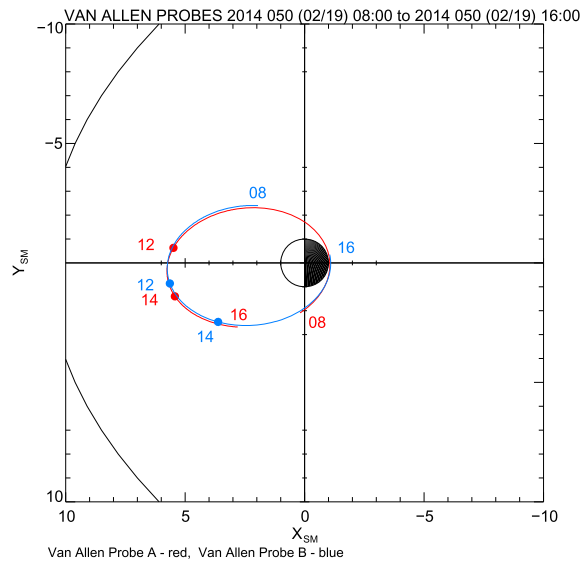


Figure 2. Dst index on 19 February 2014 from World Data Center for Geomagnetism, Kyoto.

Figure 4 (right column) shows time series of components of the magnetic field, with labels B_a , B_r , B_p , and B_T denoting azimuthal, radial, parallel, and total intensity. There is a clear B_p (or B_T) quasiperiodic oscillation between 1250 UT and 1350 UT with ≈ 600 s period and ≈ 40 nT peak-to-peak value. The B_p oscillation dominates in this interval. The solid and dashed lines in Figure 4 (right column) indicate the time of B_p minima and maxima, respectively, and as explained below are useful when comparing the phase relationship between B_p and particle fluxes. We primarily select five minima between 1250 UT and 1350 UT, excluding small dips at 1313 UT and 1325 UT in consideration of amplitudes and periods. Then we select only one maximum between two minima, which is the largest point at its interval, and find a preceding maximum at 1257 UT and a succeeding maximum at 1344 UT.

Omnidirectional differential fluxes of electrons and protons from MagEIS and REPT are plotted in Figure 5 (left column). For electrons, the energy range is from 79.80 keV to 2.85 MeV, while for protons it is from 82.85 keV to 636.18 keV. The energy spectrum has a negative slope in both cases, whereas the overall trend fluxes remain almost constant because the change of L^* is small. The phase of the particle flux oscillations is similar across all energies after 1250 UT, indicating that the modulation process covers a wide energy band. The solid and dashed lines in Figure 5 (left column) refer to times when B_p reaches minima and maxima, using the same

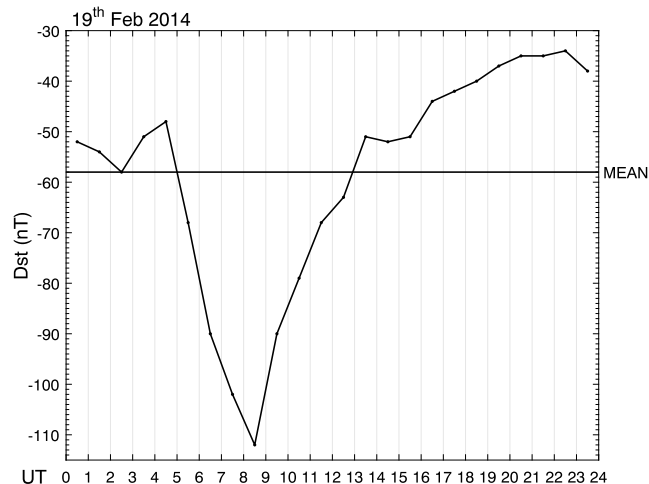


Figure 3. Van Allen Probes orbits between 0800 and 1600 UT on 19 February 2014. The red line represents Van Allen Probe A and the blue line represents Van Allen Probe B. The “12” means 1200 UT.

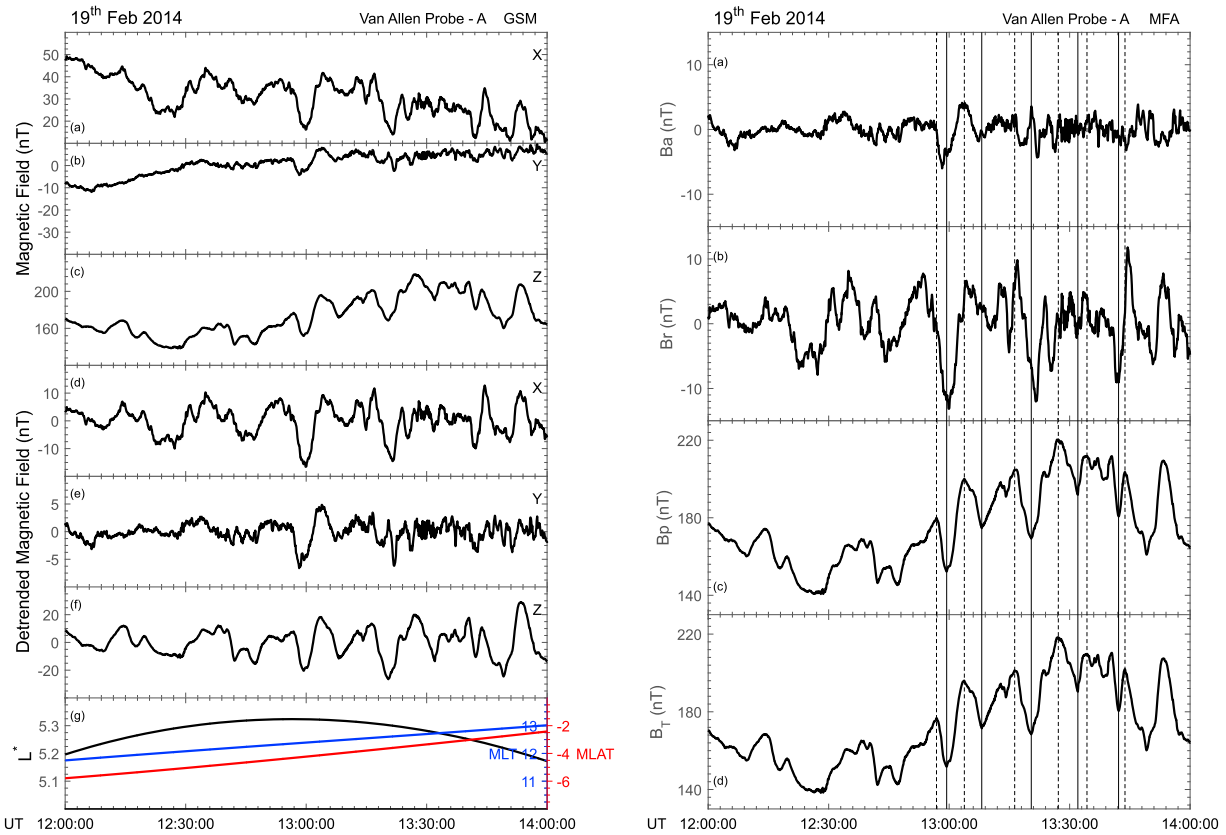


Figure 4. (left column) Van Allen Probe A magnetic field in GSM coordinates and location of spacecraft between 1200 and 1400 UT on 19 February 2014. B_x , B_y , and B_z are plotted at Figures 4a–4c (left column) in order and Figures 4d–4f (left column) contain detrend magnetic field corresponding to Figures 4a–4c (left column), respectively. (g, left column) The spacecraft magnetic location in magnetosphere. (right column) Van Allen Probe A magnetic field in MFA coordinates. From Figures 4a to 4d (right column) azimuthal, radial, compressional, and total intensities are plotted in turn. Solid and dashed lines represent the time of B_p minima and maxima, respectively.

nomenclature as in Figure 4 (right column). It is clear that for each energy channel the particle flux peaks near the solid lines, implying a strong correlation between particle fluxes and the magnetic compressional mode.

To obtain the long-term trend of each channel, we apply a 20 min running mean to the flux data. Then we divide the flux data by the long-term trend ($\text{Flux} / \langle \text{Flux} \rangle_{20\text{min}}$) of each channel to obtain the relative amplitude of the oscillation. This is shown in Figure 5 (right column). Note that we separate different channels by adding different integers to avoid lines overlapping. It is obvious from Figure 5 (right column) that the compressional wave modulation is more effective for higher energy particles, because amplitudes of oscillations are larger at higher channels.

3.3. Pitch Angle Distribution and Peak-to-Valley Ratios

Our analysis confirms that Van Allen Probe A has observed a compressional wave modulation phenomenon. We now turn to an analysis of data from Van Allen Probe B, which is ≈ 1 h ahead of Van Allen Probe A, with L^* decreasing from 5.35 to 4.26 and MLAT increasing from -7.15 to -3.14 . Figures 6a and 6b show B_p for Van Allen Probe A and B, respectively, while Figures 6c and 6d show wavelet transforms of the data in Figures 6a and 6b. Although the two spacecraft are not far from each other, the frequencies of the B_p oscillations are quite different. The period for Van Allen Probe A is about 600 s, while the period for B is about 300 s after 1250 UT. So it is difficult to estimate the azimuthal propagating wave number m .

Pitch angle distributions of electron and proton fluxes for Van Allen Probe A (B) are plotted in Figure 7 left column (right column). From top to bottom (a) magnetic compressional component B_p , (b–e) electron, and (f–h) proton pitch angle distributions at different energies are plotted. The local pitch angle distributions peaking at $\pi/2$ are indicative of particles trapped near the magnetic equator near $L^* \approx 5$, for the magnetic latitude is only $\approx -4^\circ$ for Van Allen Probe A and $\approx -5^\circ$ for Van Allen Probe B. There is evidence for compressional

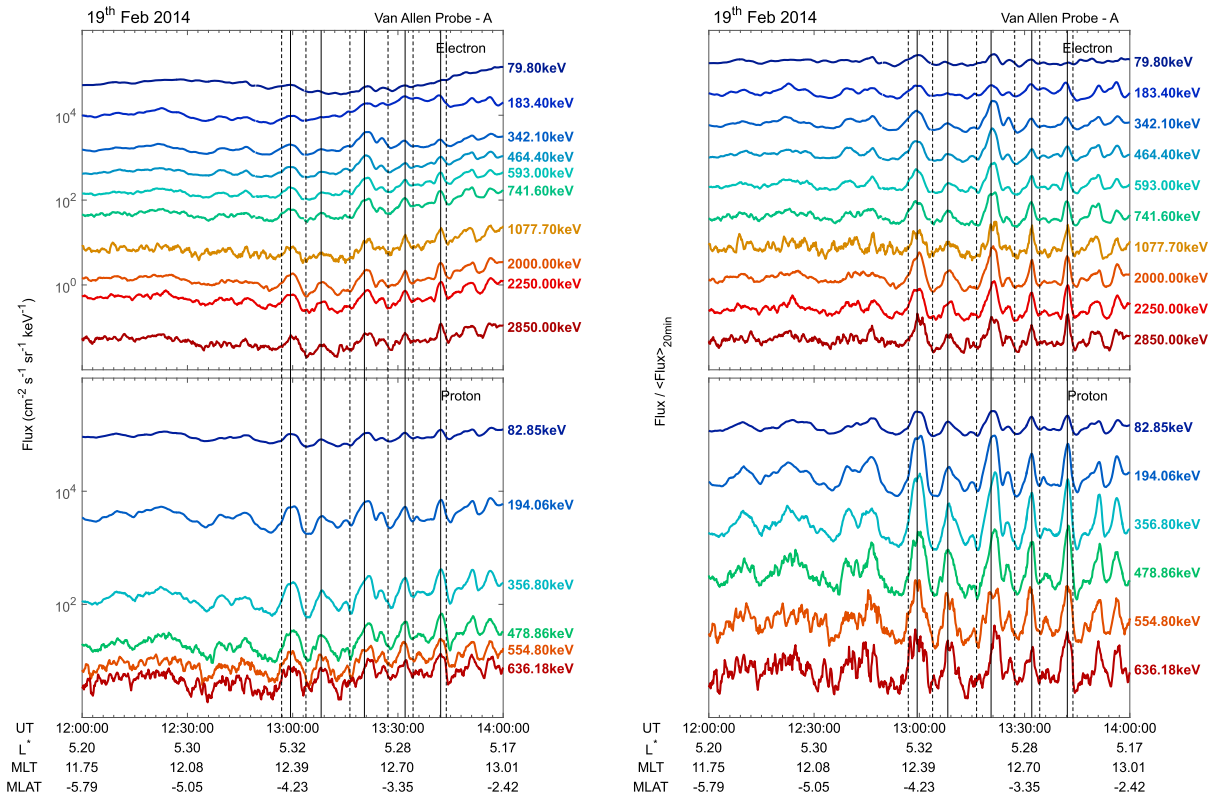


Figure 5. (left column) Van Allen Probe A MagEIS and REPT omnidirectional particle fluxes between 1200 and 1400 UT on 19 February 2014. Electron fluxes from 79.80 keV to 2.85 MeV are plotted at top panel and proton fluxes from 82.85 keV to 636.18 keV are plotted below. Solid and dashed lines represent the time of B_p minima and maxima, respectively. (right column) The same as left column but the trend is removed by dividing 20 min running mean for each channel.

wave modulation of the particle fluxes in Van Allen Probe B just as there was for probe A discussed earlier (dark blue coloring on the figure signifies zero amplitude).

The data from Van Allen Probes A and B suggest that the modulations of particle flux produced by compressional waves are stronger at higher energies. Peak-to-valley ratios can be used to quantify the strength of this modulation. For Van Allen Probe A there are five peaks of each channel in Figure 7 (right column) near the five solid lines. For each of these five peaks we use the mean of the valley values from both sides to calculate a corresponding peak-to-valley ratio. The results are plotted in Figure 8 (left column). The same procedure is applied to the observations from Van Allen Probe B and the results are plotted in Figure 8 (right column). This figure illustrates that peak-to valley ratios for both the proton and electron fluxes are larger at higher energies, although the increase is not monotonic. The peak-to-valley ratios for 636.18 keV protons show a drop compared with those for 554.80 keV protons. In Figure 7, the pitch angle distribution for the proton energy channel looks noisy due to insufficient counts, from which we conclude that data for this and higher energy channels are not reliable for further analysis. For the same reason, energy channels of electron fluxes higher than 2.85 MeV are not reliable.

4. Discussion

We have presented evidence of modulation of energetic electron and proton fluxes by compressional waves. The modulations are associated with confined directional particle fluxes at $\pi/2$ pitch angle, and out of phase oscillations between B_p and omnidirectional fluxes across a wide energy band. The observed peak-to-valley ratios demonstrate an energy dependence, although the flux oscillations show no obvious phase change with the particle energy.

To understand the flux modulations discussed in more detail, first of all we must recognize that a spacecraft-borne detector observes changes in phase space density in both momentum and configuration space. Such changes may be the result of bounce or drift-bounce resonance ULF wave-particle interactions

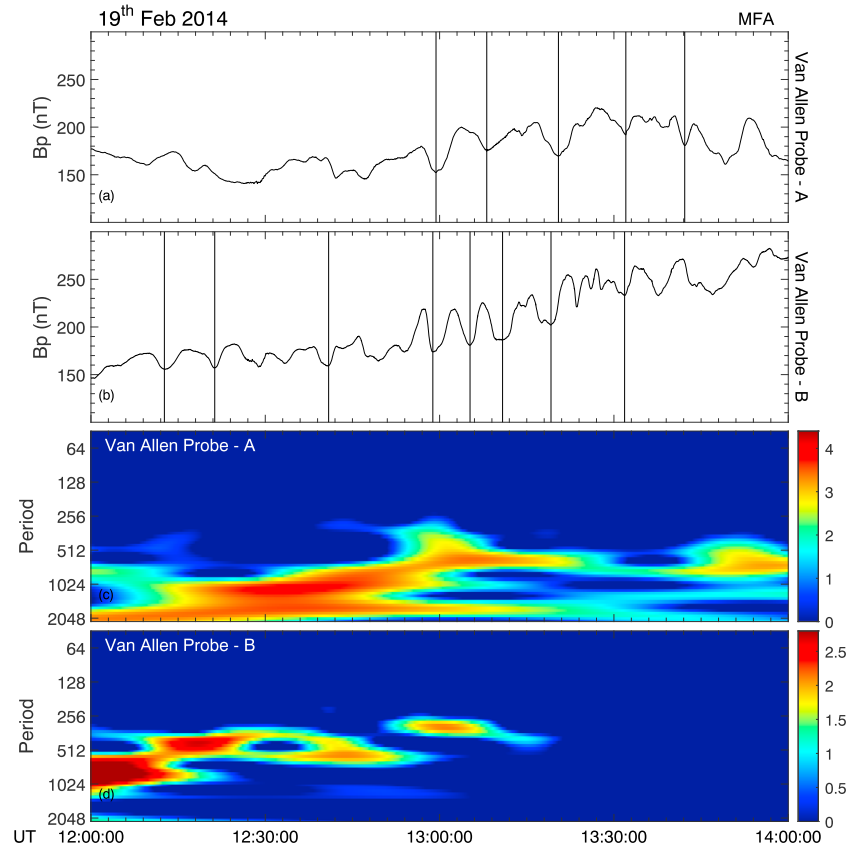


Figure 6. The comparison between compressional component of Van Allen Probes A and B. (a and b) B_p for Van Allen Probe A and B, respectively, and (c and d) wavelet transform of Figures 6a and 6b. Solid lines represent the time of B_p minima.

[Zong *et al.*, 2007, 2009; Southwood and Kivelson, 1981], in which the resonant energy channel has the largest amplitude, while adjacent energy channels show an increasing or decreasing phase change of $\pi/2$ with energy [Zhou *et al.*, 2015]. However, the case discussed in this paper does not adhere to this characteristic. The peak-to-valley ratios in Figure 8 illustrate that the amplitudes of the oscillations in electron and proton fluxes are larger at higher energies, but there is no phase difference between them.

In addition to bounce and drift-bounce resonance, it has been shown that the magnetic compressional component of ULF waves can lead to acceleration and changes in pitch angle. Lin *et al.* [1976] developed a linear theory to explain the energy and pitch angle change caused by a compressional ULF wave. Their theory predicts that the phase space density at a fixed kinetic energy and $\pi/2$ pitch angle will decrease due to betatron and Fermi deceleration in the region where the magnetic field decreases and if $\partial f / \partial(p^2) < 0$. This contradicts the observations reported in this paper, which show that the fluxes reach peaks when B_p reaches minima.

If we hypothesize that the compressional component has an azimuthal gradient, $\partial B_p / \partial \phi$, as Kivelson and Southwood [1985] did, particles will perform a radial grad-B drift. The perturbation in phase space density f produced by radial grad-B drift is given as [Kivelson and Southwood, 1985]:

$$\frac{\partial f}{\partial t} = -\frac{\partial f}{\partial L} L = \frac{\mu}{qB_e L R_E^2} \frac{\partial f}{\partial L} \frac{\partial B_p}{\partial \phi},$$

where μ is the magnetic moment, B_e is the equatorial magnetic field, R_E is the Earth's radius, and ϕ is the azimuthal angle measured positive eastward. It is clear that the electron and proton fluxes will oscillate out of phase, in contrast to what is observed. We have mentioned the observed frequencies for Van Allen Probe A and B are quite different. Thus the B_p oscillations can be expressed as

$$B_p = B_0 + b e^{im(\phi)\phi - i\omega(\phi)t} \Rightarrow \frac{\partial B_p}{\partial \phi} = b e^{im(\phi)\phi - i\omega(\phi)t} \left[im(\phi) + i \left(\frac{\partial m(\phi)}{\partial \phi} \right) \phi - i \left(\frac{\partial \omega(\phi)}{\partial \phi} \right) t \right].$$

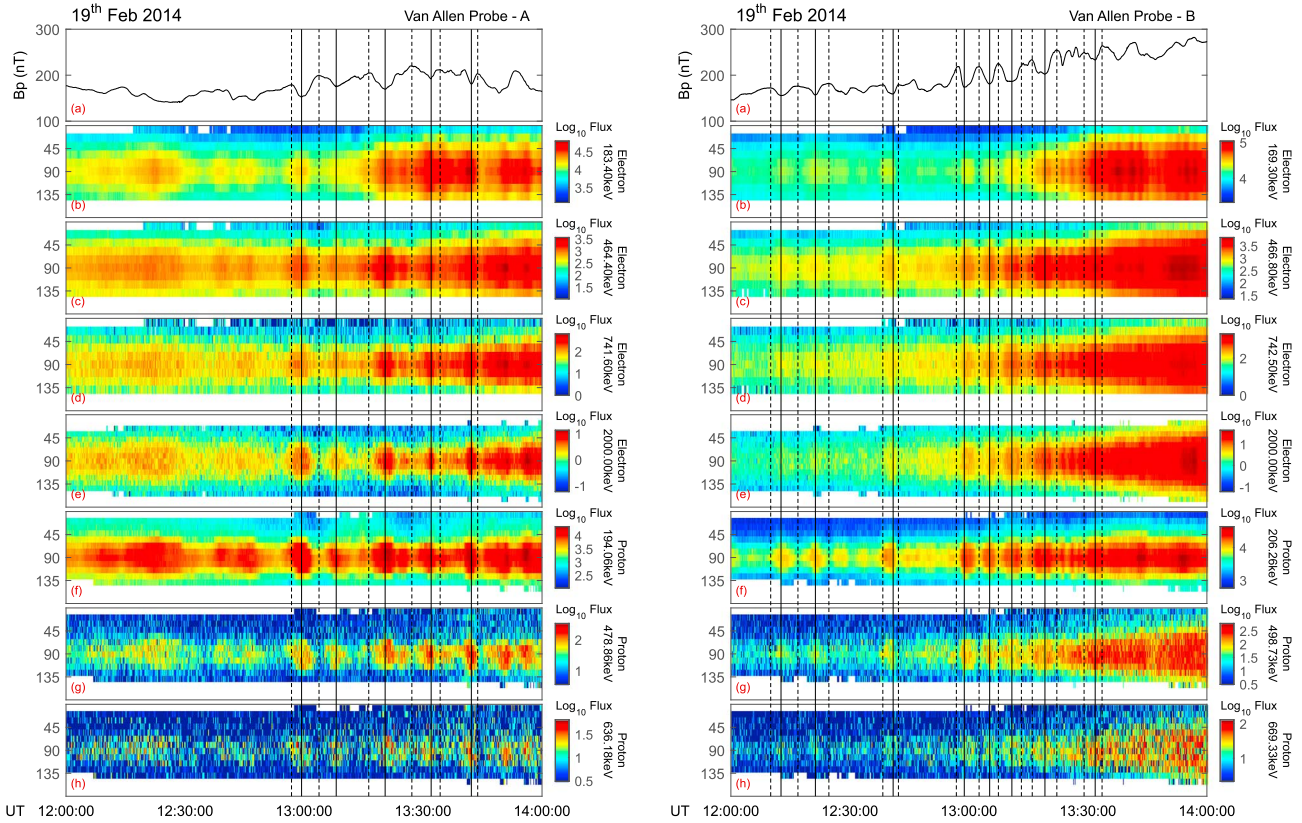


Figure 7. (left column) Van Allen Probe A compressional component and electron and proton pitch angle distributions. From top to bottom the following items are plotted: (a) magnetic compressional component, (b–e) electron pitch angle distributions at different energies, and (f–h) proton pitch angle distributions at different energies. (right column) The same as left column but for Van Allen Probe B.

Since azimuthal wave number $m(\phi)$ and angle frequency $\omega(\phi)$ is unknown, we are not able to justify if $\partial B_p / \partial \phi = 0$.

If spatial effects are important in bouncing motion, the mirror force must be considered. Trapped particles are confined near the magnetic field minimum, while particles with small pitch angle can reach the magnetic maximum. When a spacecraft travels through a magnetic field minimum, it will be near the magnetic bottle center and should detect a flux maximum [Kivelson and Southwood, 1996]. A typical mirror magnetic field is sketched in Figure 9. Consequently, the pitch angle distributions at a^* (or b^*) should be similar with distributions at a . Since the distributions at a^* (or b^*) can be deduced from in situ observations at a (or b), the similarity can be verified because the distributions at a are also observed in situ by spacecraft.

In the mirror magnetic field in Figure 9, the spacecraft will pass through a , a^* , and b alternately. The distributions at a^* and b^* could be deduced from observations at a and b under the condition that kinetic energy and magnetic moment μ (or p_{\perp}^2/B for relativistic case) are conserved. A particle with total momentum p_0 and pitch angle α_0 at (a, t_0, p_0, α_0) will arrive at (a^*, t, p, α) after some time. Based on Liouville's theorem $df/dt = 0$, the phase space density $f(t, p, \alpha)$ at a^* is equal to $f_0(t_0, p_0, \alpha_0)$ at a . Since we assume distributions are steady and energy and μ are conserved, the resulting equations are

$$\begin{cases} f(\alpha) = f_0(\alpha_0) \\ F(\alpha) = p^2 f(\alpha) = p_0^2 f_0(\alpha_0) = F_0(\alpha_0) \\ \sin \alpha = \sin \alpha_0 \sqrt{B/B_0}, \end{cases}$$

where $F(\alpha)$ and $F_0(\alpha)$ are directional flux at a^* and a , respectively, and B and B_0 are total magnetic fields.

For the event discussed in this paper, there are five magnetic minima for Van Allen Probe A corresponding to each energy channel, so we try to compare deduced pitch angle distributions with those at four magnetic

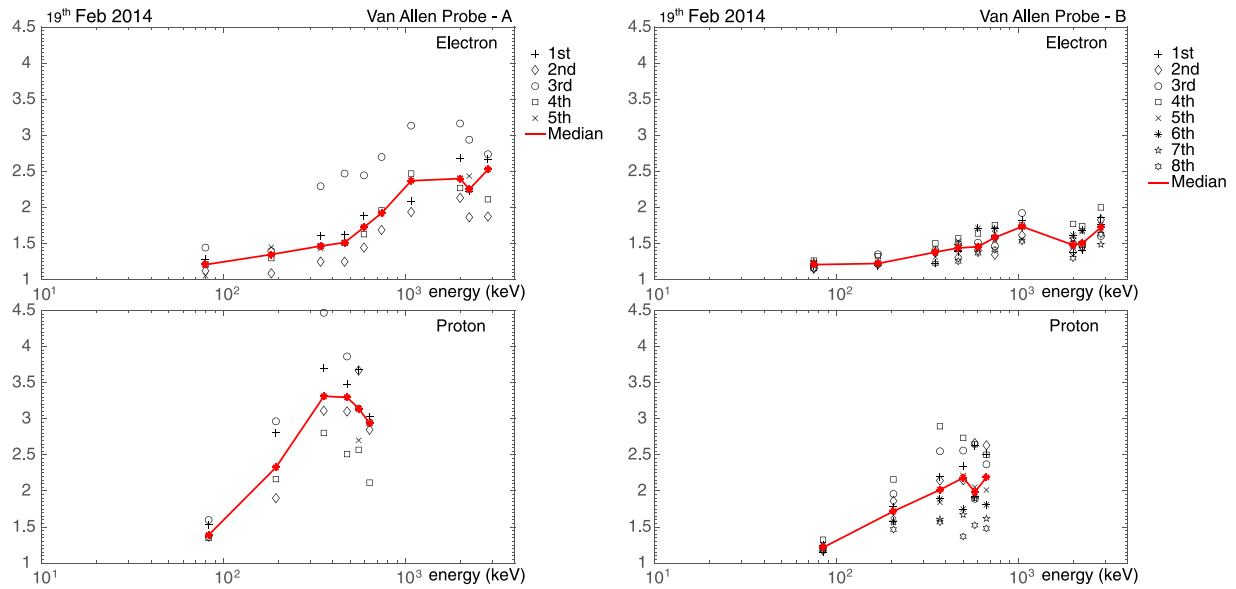


Figure 8. (left column) Peak-to-valley ratios of electron (top) and proton (bottom) residual fluxes on 19 February 2014. Five peak-to-valley ratios of each energy channel are marked by different symbols, corresponding to the five peaks near the solid lines on Figure 5 (right column). Derivation of peak-to-valley ratios is explained in the text. The red line represents medians of these five points. (right column) The same as left but for Van Allen Probe B.

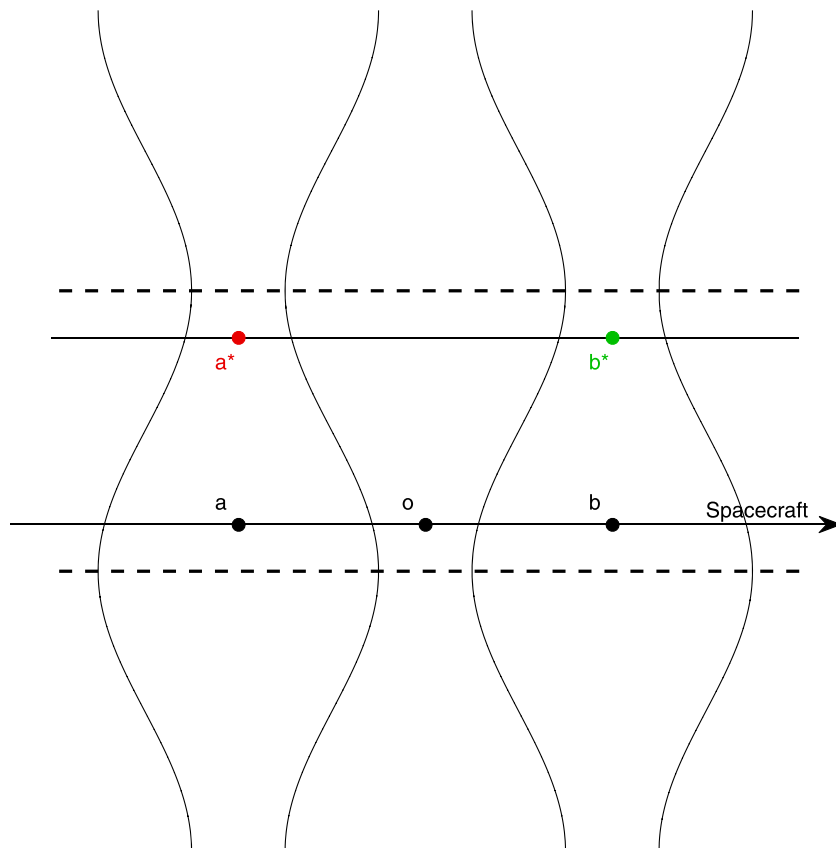


Figure 9. Schematic of mirror magnetic field in the wave static frame. An arrow line represents the spacecraft trajectory.

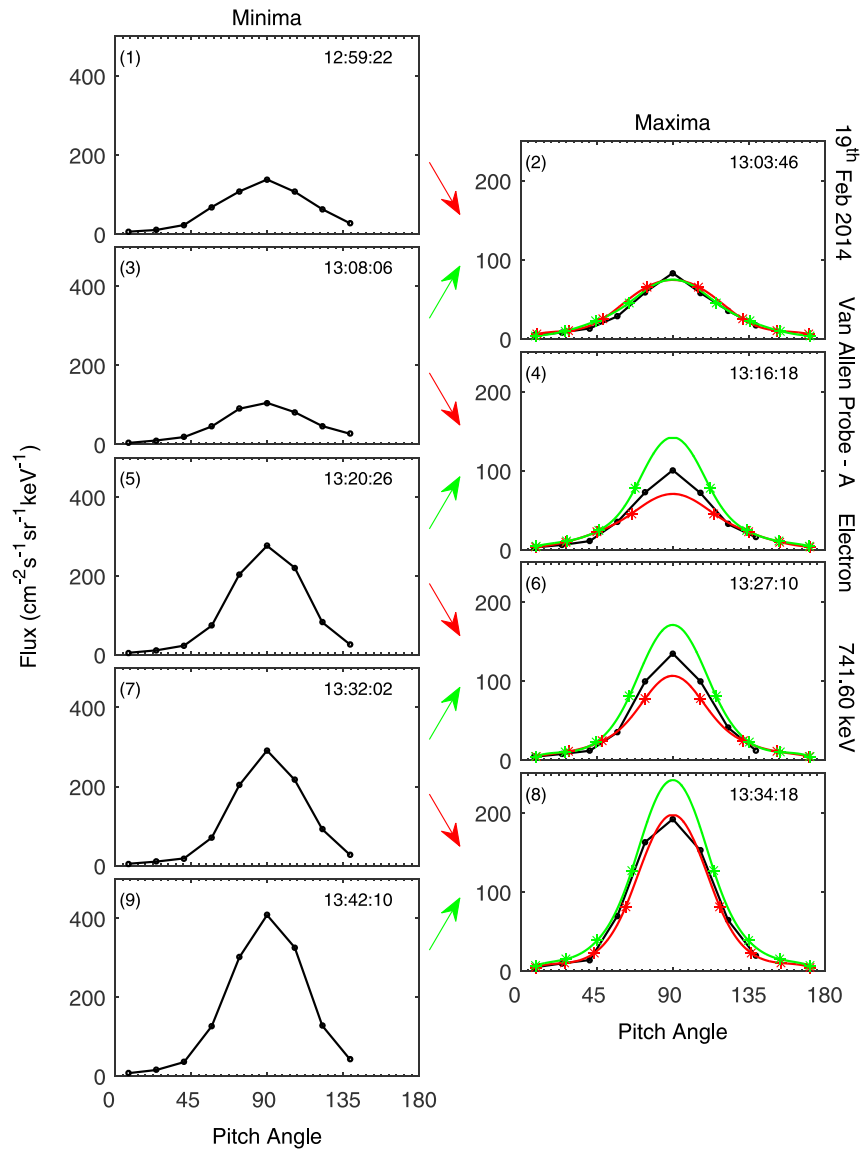


Figure 10. Van Allen Probe A observations of 741.60 keV electron pitch angle distributions. Left five panels are moments when B_p reaches minima, and right four panels are moments when B_p reaches maxima. Black lines are observations and red (green) lines are deduced distributions from preceding (succeeding) minima.

maxima. We first select 741.60 keV electron fluxes and show results in Figure 10. Figure 10 (left column) corresponds to moments when B_p reaches minima, and Figure 10 (right column) corresponds to moments when B_p reaches maxima. Black lines are observations and red (green) lines are deduced distributions from preceding (succeeding) minima. We make a cubic spline interpolation to discrete measurement data at a magnetic minimum, to get the whole distribution. Then we use the whole curve to deduce the distribution at a magnetic maximum, which is represented by a red or green line. So all pitch angles are covered, including those near $\pi/2$. All panels are numbered according to the time at which the observations are made.

In this event, Van Allen Probe A first arrives at a in Figure 9, and the observed distribution of 741.60 keV electron flux at this time is shown in panel (1) in Figure 10. Dots on the black line represent measured fluxes at centers of pitch angle bins. Then the spacecraft arrives at o and the corresponding observation is plotted in panel (2) with the black line. The distribution at a^* could be deduced from the observation at a and the result is plotted with the red line in panel (2). Red dots on the red line represent deduced values from black dots

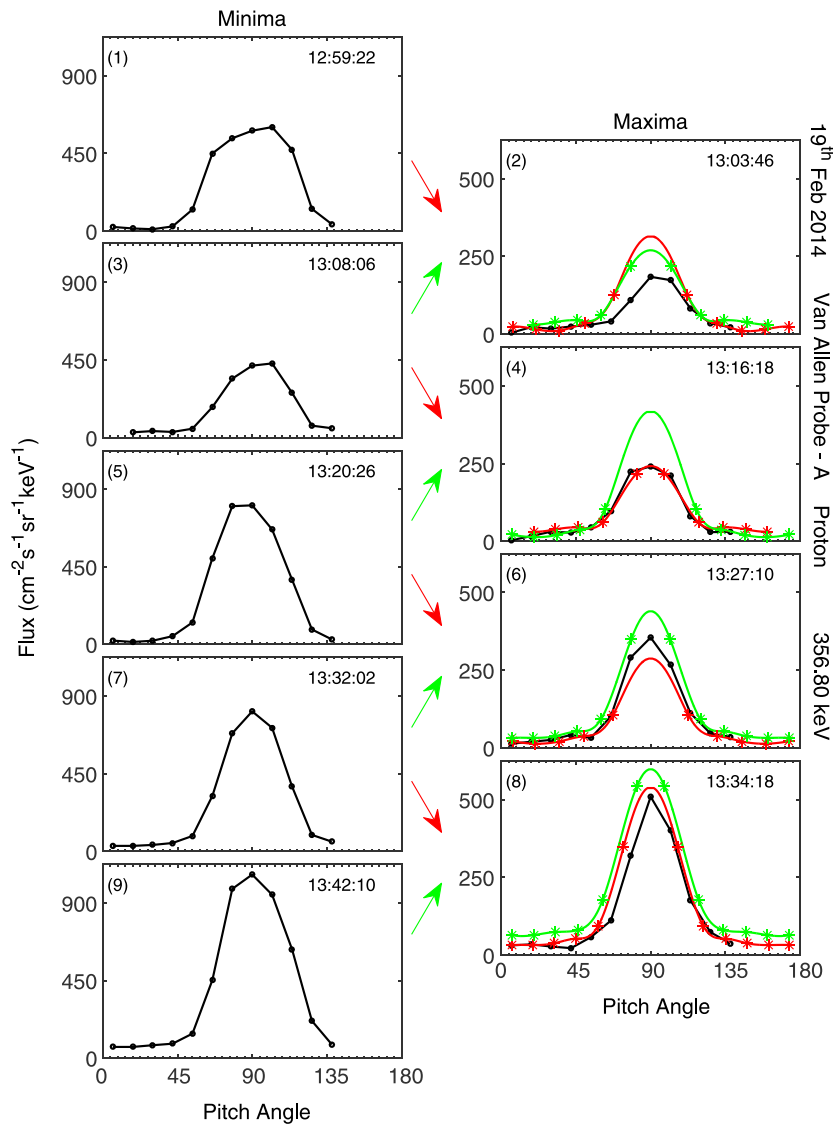


Figure 11. The same as Figure 10 but for 356.80 keV proton pitch angle distributions.

on the black line in panel (1). After that the spacecraft arrives at b . The observation is shown in panel (3), and the deduced distribution at b^* is plotted with the green line in panel (2). Green dots on the green line represent deduced values from dots on the black line in panel (3). Now we regard b as a new a and repeat the procedure until the spacecraft reaches the fifth B_p minimum. Note that red and green dots in Figure 10 (right) are directly from observed data points, but the whole curves are deduced from interpolated lines. The interpolation causes unreliability to some degree. Figure 11 is the same as Figure 10 but for 356.80 keV proton pitch angle distributions. In Figure 12 the comparison between observed electron and proton distributions and deduced ones for all pitch angle bins and energy channels at four B_p maxima are presented. The x coordinate of a data point represents the observed directional flux at a B_p maximum, i.e., at o in Figure 9, and the y coordinate is the deduced flux with the same pitch angle and energy. Also the data points are divided into two groups. The y coordinate of a red data point is the deduced flux at a^* , and that of a green data point is the deduced flux at b^* . It is clear that data points are located near the diagonal line.

Since the magnetic field B at a^* in Figure 9 is larger than the magnetic field B_0 at a , all particles at a with pitch angle smaller than a marginal value α_0^* , which is determined by $\sin \alpha_0^* = \sqrt{B_0/B}$, can reach a^* after some time. A particle with pitch angle larger than $\pi - \alpha_0^*$ can also reach a^* after a longer time. We assume the pitch angle

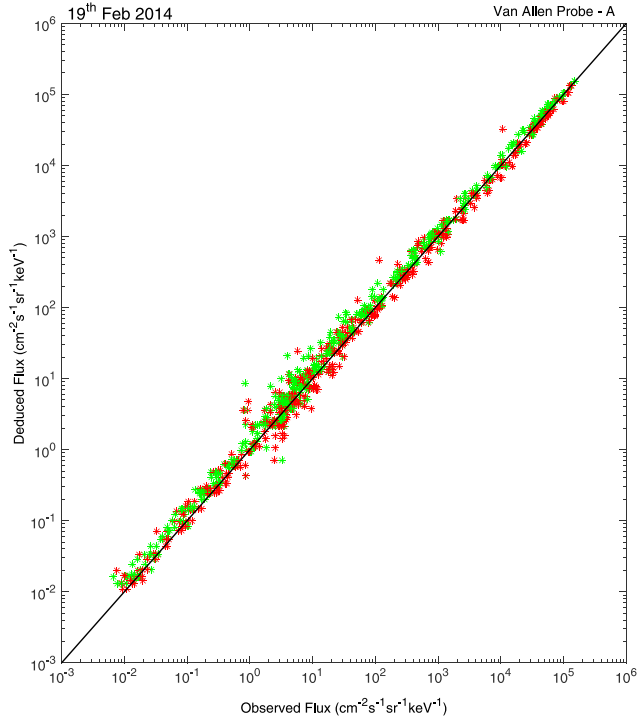


Figure 12. The comparison between observed electron and proton distributions and deduced ones for all pitch angle bins and energy channels at four B_p maxima. The x coordinate of a data point represents the observed directional flux, and the y coordinate is the deduced flux with the same pitch angle and energy. Red (green) points represent the comparison between observed distributions and deduced ones from a preceding (succeeding) magnetic minimum.

distribution is symmetric about $\pi/2$, the peak-to-valley ratio

$$\begin{aligned} \gamma &= \left[\int_0^{\pi/2} F_0(\alpha_0) \sin \alpha_0 d\alpha_0 \right] / \left[\int_0^{\pi/2} F(\alpha) \sin \alpha d\alpha \right] \\ &= \left[\int_0^{\pi/2} f_0(\alpha_0) \sin \alpha_0 d\alpha_0 \right] / \left[\int_0^{\pi/2} f(\alpha) \sin \alpha d\alpha \right] \\ &= \frac{B_0}{B} \left[\int_0^{\pi/2} f_0(\alpha_0) \sin \alpha_0 d\alpha_0 \right] / \left[\int_0^{\alpha_0} f_0(\alpha_0) \sin \alpha_0 \cos \alpha_0 d\alpha_0 / \sqrt{1 - \sin^2 \alpha_0 \frac{B}{B_0}} \right] \\ &= \left[\int_0^{\pi/2} f_0(x) \sin x dx \right] / \left[\int_0^{\pi/2} f_0[\arcsin(\sqrt{B_0/B} \sin x)] \sin x dx \right], \end{aligned}$$

where $F(\alpha) = p^2 f(\alpha)$ is the directional flux.

If the pitch angle distribution f_0 is uniform, i.e., $f_0(\alpha_0) = 1$, the peak-to-valley ratio $\gamma = 1$. Since $\arcsin(\sqrt{B_0/B} \sin x) < x$, if f_0 is peaking at $\pi/2$, i.e., $f_0(x) < f_0(y)$ when $0 \leq x < y \leq \pi/2$, $f_0[\arcsin(\sqrt{B_0/B} \sin x)] < f_0(x)$, so $\gamma > 1$. If f_0 is peaking at 0, i.e., $f_0(x) > f_0(y)$ when $0 \leq x < y \leq \pi/2$, $f_0[\arcsin(\sqrt{B_0/B} \sin x)] > f_0(x)$, so $\gamma < 1$. These results explain occurrences of in-phase and out-of-phase events refer to [Kremser et al., 1981]. For the situation that f_0 is peaking at $\pi/2$, if the pitch angle distribution is narrower, the peak-to-valley ratio γ will become larger. Normalized (divided by maximum) pitch angle distributions at different energies are plotted in Figure 13. It is clear that for both electrons and protons the normalized pitch angle distributions at lower energies are wider than those at higher energies.

It is difficult to settle whether the B_p oscillations are nonpropagating spatial structures or propagating waves, for the observed frequencies of two spacecraft are quite different. However, our analysis remains valid as long as we select a moving frame with the same azimuthal phase velocity. Both propagating compressional ULF waves and nonpropagating mirror modes can cause such a magnetic field configuration as shown in Figure 9. Although we cannot exclude the nonpropagating mirror modes, we tend to believe the wave is propagating compressional ULF waves. The mirror instability occurs in high- β ($\beta > 1$) plasma [Kivelson and Southwood,

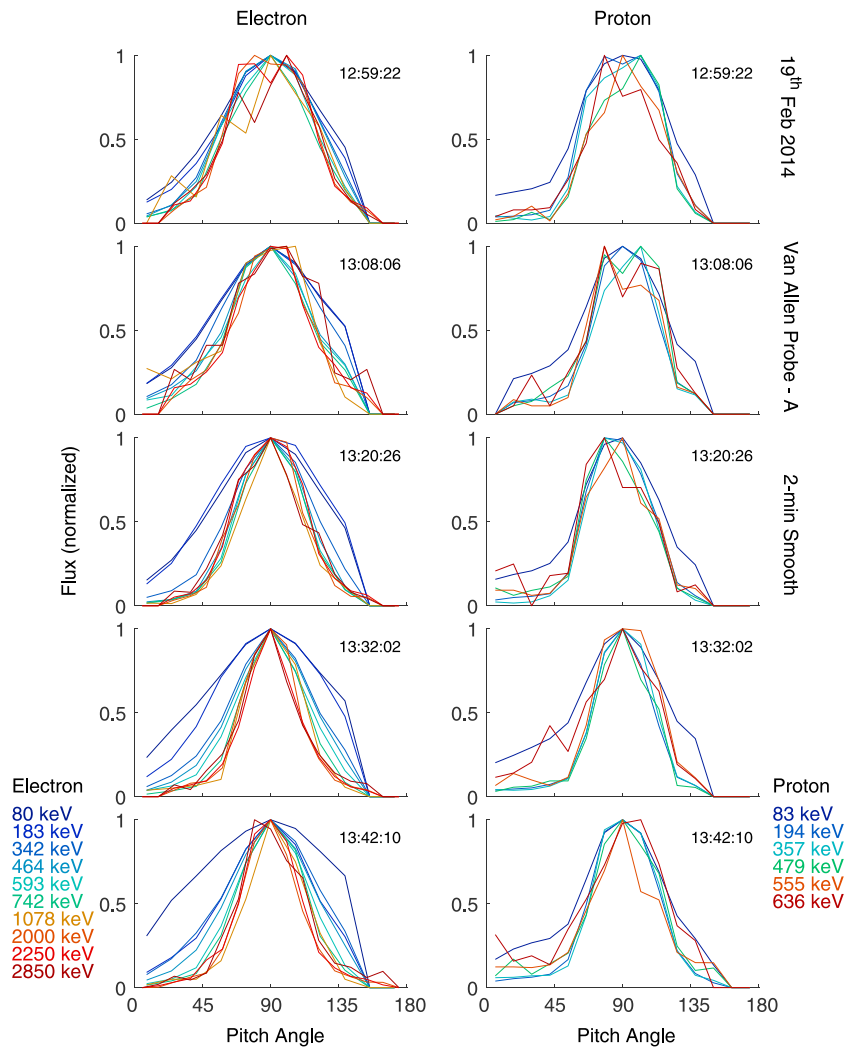


Figure 13. Van Allen Probe A observations of (left) electron and (right) proton pitch angle distributions. Five rows correspond to five B_p minima, and lines with different color represent different energies as shown in the legend. Distributions are normalized by dividing a maximum.

1996], but the criterium is unlikely to be satisfied on this dayside inner magnetospheric region. Previous work shows that the magnetic perturbations of mirror mode tend to be comparable to the total magnetic field strength that $\delta B_t/B_t \approx 1$, but for the event presented in this paper it is only about 0.2. Drift mirror waves are also regarded as compressional waves [Sibeck *et al.*, 2012], so the nonpropagating mirror modes can be regarded as special cases. The mirror mode modulation of energetic particles is also the result of mirror effect [Kivelson and Southwood, 1996], so we use the same terminology.

We ascribe the compressional wave modulation phenomenon to the mirror effect; however, the mechanism to produce the compressional waves is beyond the scope of the present paper. In particular the mirror effect can trap relativistic electrons even if the decrease of B_p is only $\approx 20\%$. However, the gyroradius of 636.18 keV proton is about 502 km for $B \approx 200$ nT. The curvature parameter κ is around 2, which is defined as $\kappa = \sqrt{R_{\min}/\rho_{\max}}$ where R_{\min} is the minimum radius of curvature of the magnetic field and ρ_{\max} is the maximum Larmor radius for a 636.18 keV proton [Büchner and Zelenyi, 1989]. If the energy is higher and the gyroradius is larger, this local structure is not expected to trap particles and so the modulation effect will reduce. However, we can hardly illustrate it from observations because the pitch angle distributions for this and higher energy channels are not reliable, as mentioned above. For electrons, we have also suggested that pitch angle distributions for 2.85 MeV and higher energy channels are not reliable, but the gyroradius of a 2.85 MeV electron is only about 55 km for $B \approx 200$ nT, which is far less than the scale of the mirror magnetic structure.

5. Summary

A compressional ULF wave modulation event in the dayside magnetosphere has been reported and the following characteristics have been explained:

1. Trapped electron fluxes from 79.80 to 2.85 MeV and proton fluxes from 82.85 to 636.18 keV oscillate out of phase with the magnetic compressional component. Pitch angle distributions peak at $\pi/2$ for all energies.
2. Peak-to-valley ratios are used to show that the amplitude of electron and proton flux modulations is larger at higher energies than at lower energies.
3. After examining several possible mechanisms, we attribute the observed particle flux modulations to the mirror effect along the field and suggest this effect can trap relativistic electrons for energies up to 2.85 MeV.
4. The fact that peak-to-valley ratios are larger at higher energies is explained by the pitch angle distributions becoming narrower.
5. Although relativistic electron particle fluxes can be modulated by compressional waves, we suggest that the large gyroradius of protons with energies in excess of 636.18 keV is so large that the mirror effect is reduced.

Acknowledgments

This work was supported by National Natural Science Foundation of China (41421003) and Major Project of Chinese National Programs for Fundamental Research and Development (2012CB825603). We acknowledge Space Physics Data Facility, Goddard Space Flight Center (<http://cdaweb.gsfc.nasa.gov/>) for providing Solar Wind and IMF data. R. Rankin acknowledges financial support from NSERC and the Canadian Space Agency.

References

- Baker, D., et al. (2012), The Relativistic Electron-Proton Telescope (REPT) instrument on board the Radiation Belt Storm Probes (RBSP) spacecraft: Characterization of Earth's radiation belt high-energy particle populations, in *The Van Allen Probes Mission*, pp. 337–381, Springer, Netherlands.
- Blake, J., et al. (2013), The Magnetic Electron Ion Spectrometer (MAGEIS) instruments aboard the Radiation Belt Storm Probes (RBSP) spacecraft, *Space Sci. Rev.*, *179*(1–4), 383–421.
- Brown, W., L. Cahill, L. Davis, C. McIlwain, and C. Roberts (1968), Acceleration of trapped particles during a magnetic storm on April 18, 1965, *J. Geophys. Res.*, *73*(1), 153–161.
- Büchner, J., and L. M. Zelenyi (1989), Regular and chaotic charged particle motion in magnetotail-like field reversals: 1. Basic theory of trapped motion, *J. Geophys. Res.*, *94*(A9), 11,821–11,842.
- Hasegawa, A. (1969), Drift mirror instability in the magnetosphere, *Phys. Fluids*, *12*(12), 2642–2650.
- Higbie, P., D. Baker, R. Zwickl, R. Belian, J. Asbridge, J. Fennell, B. Wilken, and C. Arthur (1982), The global Pc 5 event of November 14–15, 1979, *J. Geophys. Res.*, *87*(A4), 2337–2345.
- Jacobs, J., Y. Kato, S. Matsushita, and V. Troitskaya (1964), Classification of geomagnetic micropulsations, *J. Geophys. Res.*, *69*(1), 180–181.
- Kivelson, M. G., and D. J. Southwood (1985), Charged particle behavior in low-frequency geomagnetic pulsations, 4. Compressional waves, *J. Geophys. Res.*, *90*, 1486–1498.
- Kivelson, M. G., and D. J. Southwood (1996), Mirror instability II: The mechanism of nonlinear saturation, *J. Geophys. Res.*, *101*(A8), 17,365–17,371.
- Kletzing, C., et al. (2013), The electric and magnetic field instrument suite and integrated science (emfisis) on rbps, *Space Sci. Rev.*, *179*.
- Kremser, G., A. Korth, J. Fejer, B. Wilken, A. Gurevich, and E. Amata (1981), Observations of quasi-periodic flux variations of energetic ions and electrons associated with Pc 5 geomagnetic pulsations, *J. Geophys. Res.*, *86*(A5), 3345–3356.
- Lanzerotti, L., A. Hasegawa, and C. MacLennan (1969), Drift mirror instability in the magnetosphere: Particle and field oscillations and electron heating, *J. Geophys. Res.*, *74*(24), 5565–5578.
- Lee, D.-H., and R. L. Lysak (1989), Magnetospheric ULF wave coupling in the dipole model: The impulsive excitation, *J. Geophys. Res.*, *94*(A12), 17,097–17,103.
- Lepping, R., et al. (1995), The wind magnetic field investigation, *Space Sci. Rev.*, *71*(1–4), 207–229.
- Lin, C. S., G. K. Parks, and J. R. Winckler (1976), The 2- to 12-min quasi-periodic variation of 50- to 1000-keV trapped electron fluxes, *J. Geophys. Res.*, *81*(25), 4517–4523.
- Nagano, H., and T. Araki (1983), Long-duration Pc5 pulsations observed by geostationary satellites, *Geophys. Res. Lett.*, *10*(9), 908–911.
- Ogilvie, K., et al. (1995), SWE, a comprehensive plasma instrument for the Wind spacecraft, *Space Sci. Rev.*, *71*(1–4), 55–77.
- Rae, I. J., I. R. Mann, C. E. Watt, L. M. Kistler, and W. Baumjohann (2007), Equator-S observations of drift mirror mode waves in the dawnside magnetosphere, *J. Geophys. Res.*, *112*(A11), A11203, doi:10.1029/2006JA012064.
- Sibeck, D., G. Korotova, D. Turner, V. Angelopoulos, K.-H. Glaßmeier, and J. McFadden (2012), Frequency doubling and field-aligned ion streaming in a long-period poloidal pulsation, *J. Geophys. Res.*, *117*, A11215, doi:10.1029/2011JA017473.
- Sonnerup, B., L. Cahill, and L. Davis (1969), Resonant vibration of the magnetosphere observed from Explorer 26, *J. Geophys. Res.*, *74*(9), 2276–2288.
- Southwood, D. J., and M. G. Kivelson (1981), Charged particle behavior in low-frequency geomagnetic pulsations 1. Transverse waves, *J. Geophys. Res.*, *86*(A7), 5643–5655.
- Southwood, D. J., and M. G. Kivelson (1993), Mirror instability: 1. Physical mechanism of linear instability, *J. Geophys. Res.*, *98*(A6), 9181–9187.
- Stewart, B. (1861), On the great magnetic disturbance which extended from August 28 to September 7, 1859, as recorded by photography at the Kew Observatory, *Philos. Trans. R. Soc.*, *151*, 423–430.
- Takahashi, K., P. R. Higbie, and D. N. Baker (1985), Azimuthal propagation and frequency characteristic of compressional Pc 5 waves observed at geostationary orbit, *J. Geophys. Res.*, *90*(A2), 1473–1485.
- Takahashi, K., R. Lopez, R. McEntire, L. Zanetti, L. Kistler, and F. Ipavich (1987), An eastward propagating compressional Pc 5 wave observed by AMPTE/CCE in the postmidnight sector, *J. Geophys. Res.*, *92*(A12), 13,472–13,484.
- Walker, A., R. Greenwald, A. Korth, and G. Kremser (1982), STARE and GEOS 2 observations of a storm time Pc 5 ULF pulsation, *J. Geophys. Res.*, *87*(A11), 9135–9146.
- Zhou, X.-Z., Z.-H. Wang, Q.-G. Zong, S. G. Claudepierre, I. R. Mann, M. G. Kivelson, V. Angelopoulos, Y.-X. Hao, Y.-F. Wang, and Z.-Y. Pu (2015), Imprints of impulse-excited hydromagnetic waves on electrons in the Van Allen radiation belts, *Geophys. Res. Lett.*, *42*, 6199–6204, doi:10.1002/2015GL064988.

- Zhu, X., and M. G. Kivelson (1994), Compressional ULF waves in the outer magnetosphere: 2. A case study of Pc 5 type wave activity, *J. Geophys. Res.*, *99*(A1), 241–252.
- Zong, Q.-G., et al. (2007), Ultralow frequency modulation of energetic particles in the dayside magnetosphere, *Geophys. Res. Lett.*, *34*(12), L12105, doi:10.1029/2007GL029915.
- Zong, Q.-G., X.-Z. Zhou, Y. Wang, X. Li, P. Song, D. Baker, T. Fritz, P. Daly, M. Dunlop, and A. Pedersen (2009), Energetic electron response to ULF waves induced by interplanetary shocks in the outer radiation belt, *J. Geophys. Res.*, *114*, A10204, doi:10.1029/2009JA014393.